Morphology of residually stressed tubular tissues: Beyond the elastic multiplicative decomposition

P. Ciarletta [a,b,*], M. Destrade [c,d], A.L. Gower [c,e], M. Taffetani [b,f]

[a] *Sorbonne Universités, UPMC Univ Paris 06, CNRS, UMR 7190, Institut Jean Le Rond d'Alembert, F-75005 Paris, France*
[b] *MOX – Politecnico di Milano, piazza Leonardo da Vinci 32, 20133 Milano, Italy*
[c] *School of Mathematics, Statistics and Applied Mathematics, NUI Galway, University Road, Galway, Ireland*
[d] *School of Mechanical and Materials Engineering, University College Dublin, Belfield, Dublin 14, Ireland*
[e] *School of Mathematics, University of Manchester, Oxford Road, Manchester M13 9PL, UK*
[f] *Mathematical Institute, University of Oxford, Oxford OX2 6GG, UK*

ARTICLE INFO

ABSTRACT

Many interesting shapes appearing in the biological world are formed by the onset of mechanical instability. In this work we consider how the build-up of residual stress can cause a solid to buckle. In all past studies a fictitious (virtual) stress-free state was required to calculate the residual stress. In contrast, we use a model which is simple and allows the prescription of any residual stress field.

We specialize the analysis to an elastic tube subject to a two-dimensional residual stress, and find that incremental wrinkles can appear on its inner or its outer face, depending on the location of the highest value of the residual hoop stress. We further validate the predictions of the incremental theory with finite element simulations, which allow us to go beyond this threshold and predict the shape, number and amplitude of the resulting creases.

© 2016 Elsevier Ltd. All rights reserved.

1. Introduction

The development of living materials interrelates biological processes at the molecular level and feedback mechanisms with the external environment. As a result, living matter is regulated by mechano-sensing receptors (e.g. integrins, cadherins) at the cellular level, which determine the behavior at the macroscopic level. In particular, it is now well-acknowledged that a mechanical coupling drives the material properties of an adult tissue, which are somewhat optimized for their physiological functions (Bao and Suresh, 2003). This mechanical feedback produces *residual stresses* within the material, which we define as the self-equilibrated stresses inside the body which persist in the absence of both external loads and geometrical constraints. This set-up happens for example in arteries, mechanically acting as soft thick tubes subjected to an internal blood pressure. Differential growth inside the artery produces an inhomogeneous residual stress, which tends to establish an optimal structural response to the internal pressure (Chuong and Fung, 1986).

As the growth creates residual stress, the residual stress in turn can cause the tissue to become unstable and wrinkle or crease. One motivation for this work is to discover how much can we learn about the residual stresses from observing the formation (or avoidance) of wrinkles and creases.

---

* Corresponding author.
  E-mail addresses: pasquale.ciarletta@polimi.it, pasquale.ciarletta@upmc.fr (P. Ciarletta).

From a modeling standpoint, much work has been done by Hoger (1985, 1986, 1993, 1996) and Johnson and Hoger (1993) in the last decades to define a hyperelastic constitutive theory of soft materials with residual stresses. Hoger and co-workers proposed a multiplicative decomposition (Rodriguez et al., 1994; Skalak et al., 1996) to deal with volumetric growth in living materials, based on the framework introduced by Kroner and Lee for plasticity. Using a virtual state for the kinematic description of the grown material, these seminal articles demonstrated that if such a state is geometrically incompatible, then residual stresses can be calculated by considering the elastic strains which are necessary to restore compatibility of the spatial configuration. This approach has proved very popular and successful in the last couple of decades, inspiring an entire generation of researchers to work on the biomechanics of growth and remodeling. Just to mention a few applications, this theoretical framework has been extended to define the required thermo-mechanical restrictions on the stress-dependent evolution laws, and has powered the rise of morphoelastic theories, which deal with the analysis of the influence of mechanical effects on pattern selection in growing tissues.

Although Hoger's theoretical framework provides an elegant description of the residual stress distribution inside a material, its main drawback is that it refers to both an unloaded residually stressed configuration and a grown virtual state which are not always accessible in experimental practice. In general this virtual state corresponds to the collection of stress-free states of each volume element of the initially stressed material. In only very few special cases can such a state be referred to as a configuration and be attained in physical practice, e.g. by cutting the material to remove the pre-stresses. Furthermore, recent experimental studies have demonstrated that the distribution of the residual stresses in living materials is very complex and mostly three-dimensional. In practice, it is not possible to release all residual stresses by making cuts along preferred directions, and thus it is rarely possible to properly identify the virtual state.

In this work we aim at extending the existing theoretical framework by working with a constitutive model which describes the distribution of the residual stresses in living materials without introducing any virtual state or natural configuration. In Section 2, we introduce the theory of initial stresses in elastic solids and propose a novel constitutive law for the strain energy function taking into account a functional dependence on both the elastic strains and the residual stresses. In Section 3, we apply our constitutive theory to incompressible, hyperelastic tubular tissues. In particular, we use the theory of incremental deformations superposed on finite fields to study the stability of the residually stressed configuration in circular tubes. The incremental boundary value problem is then solved for three representative classes of residual stress distributions. In Section 4 we propose a finite element implementation of the model, and perform post-buckling simulations to study the bifurcated morphology of the residually stressed configurations. There we uncover the transition from wrinkles to creases (or 'folds'). Finally in Section 5, we provide a critical discussion on the results of this work together with some concluding remarks.

2. Hyperelastic theory of residual stresses

Let $\mathcal{B}_\tau$ be the region occupied by a soft material in its reference configuration. Denoting by $\mathbf{X}$ the material position in $\mathcal{B}_\tau$, we assume that the body is subjected to a residual stress $\boldsymbol{\tau} = \boldsymbol{\tau}(\mathbf{X})$ in this configuration. It must be symmetric to satisfy the balance of angular momentum, while the balance of linear momentum in quasi-static conditions reads:

$$\text{Div}\,\boldsymbol{\tau} = \mathbf{0} \quad \text{in } \mathcal{B}_\tau, \tag{1}$$

where Div is the material divergence. We apply the zero-traction boundary conditions

$$\boldsymbol{\tau}\mathbf{N} = \mathbf{0} \quad \text{in } \partial\mathcal{B}_\tau, \tag{2}$$

where $\partial\mathcal{B}_\tau$ is the boundary of the body $\mathcal{B}_\tau$, and $\mathbf{N}$ is its outer unit normal.

An important consequence of Eqs. (1) and (2) is that the residual stress $\boldsymbol{\tau}$ must be inhomogeneous and have zero average over the volume in $\mathcal{B}_\tau$,

$$\int_{\mathcal{B}_\tau} \boldsymbol{\tau}\, dv = \mathbf{0}, \tag{3}$$

which can be shown by applying a version of the mean value theorem (Hoger, 1985).

Let us now consider that the body can be elastically deformed to a new configuration $\mathcal{B}$, so that a mapping $\chi: \mathcal{B}_\tau \to \mathcal{B}$ defines the spatial position $\mathbf{x} = \chi(\mathbf{X})$ and $\mathbf{F} = \partial\chi/\partial\mathbf{X}$ is the deformation gradient. Assuming that the body is perfectly elastic, it is possible to define a strain energy density Ψ per unit of reference volume. Since the body is residually stressed, Ψ must be necessarily inhomogeneous, so we assume the functional dependence $\Psi = \Psi(\mathbf{F}, \boldsymbol{\tau})$. Assuming that the body is incompressible, i.e. $J = \det \mathbf{F} = 1$, the first Piola–Kirchoff $\mathbf{P}$ and Cauchy $\boldsymbol{\sigma}$ stress tensors are

$$\mathbf{P} = \frac{\partial\Psi}{\partial\mathbf{F}}(\mathbf{F}, \boldsymbol{\tau}) - p\mathbf{F}^{-1}, \quad \boldsymbol{\sigma} = \mathbf{F}\mathbf{P}, \tag{4}$$

where p is the Lagrange multiplier associated with the internal constraint of incompressibility. When there is no deformation ($\mathbf{F} = \mathbf{I}$), this equation must recover the residual stress $\boldsymbol{\tau}$ for consistency. Hence, evaluating Eq. (4) in $\mathcal{B}_\tau$ by setting $\mathbf{F} = \mathbf{I}$, we derive a connection for the residual stress,

$$\tau = \frac{\partial \Psi}{\partial \mathbf{F}}(\mathbf{I}, \tau) - p_\tau \mathbf{I},\tag{5}$$

where $\mathbf{I}$ is the identity matrix and p_τ is the value of p in $\mathcal{B}_\tau$.

The presence of residual stress generally introduces anisotropy in the material response, but if we assume that there is no other source of anisotropy then the strain energy density Ψ should depend on the left Cauchy-Green strain tensor $\mathbf{C} = \mathbf{F}^T\mathbf{F}$ and τ only. Further, it can be shown (Shams et al., 2011) that Ψ depends only on the principal invariants I_j and $I_{\tau j}(j = 1, 2, 3)$ of $\mathbf{C}$ and τ, respectively,

$$I_1 = \mathrm{tr}\mathbf{C}, \quad I_2 = \tfrac{1}{2}[(I_1^2 - \mathrm{tr}(\mathbf{C}^2)], \quad I_3 = \det \mathbf{C},\tag{6}$$

$$I_{\tau 1} = \mathrm{tr}\tau, \quad I_{\tau 2} = \tfrac{1}{2}[(I_{\tau 1}^2 - \mathrm{tr}(\tau^2)]), \quad I_{\tau 3} = \det \tau,\tag{7}$$

and on the combined invariants J_i ($i = 1, \ldots, 4$),

$$J_1 = \mathrm{tr}(\tau\mathbf{C}), \quad J_2 = \mathrm{tr}(\tau\mathbf{C}^2), \quad J_3 = \mathrm{tr}(\tau^2\mathbf{C}), \quad J_4 = \mathrm{tr}(\tau^2\mathbf{C}^2).\tag{8}$$

Writing $\Psi = \Psi(I_j, I_{\tau j}, J_i)$, Eq. (4) for the Cauchy stress of an incompressible material becomes

$$\boldsymbol{\sigma} = 2\frac{\partial \Psi}{\partial I_1}\mathbf{B} + 2\frac{\partial \Psi}{\partial I_2}(I_1\mathbf{B} - \mathbf{B}^2) - p\mathbf{I} + 2\frac{\partial \Psi}{\partial J_1}\boldsymbol{\Sigma} + 2\frac{\partial \Psi}{\partial J_2}(\boldsymbol{\Sigma}\mathbf{B} + \mathbf{B}\boldsymbol{\Sigma}) + 2\frac{\partial \Psi}{\partial J_3}\boldsymbol{\Sigma}\mathbf{B}^{-1}\boldsymbol{\Sigma} + 2\frac{\partial \Psi}{\partial J_4}(\boldsymbol{\Sigma}\mathbf{B}^{-1}\boldsymbol{\Sigma}\mathbf{B} + \mathbf{B}\boldsymbol{\Sigma}\mathbf{B}^{-1}\boldsymbol{\Sigma}),\tag{9}$$

where $\mathbf{B} = \mathbf{F}\mathbf{F}^T$ and $\boldsymbol{\Sigma} \equiv \mathbf{F}\tau\mathbf{F}^T$. Recalling the required connection for the residual stresses in Eq. (5), in the reference configuration, i.e. for $\mathbf{F} = \mathbf{I}$, the following conditions must hold:

$$2\frac{\partial \Psi}{\partial I_1} + 4\frac{\partial \Psi}{\partial I_2} - p_\tau = 0, \quad 2\frac{\partial \Psi}{\partial J_1} + 4\frac{\partial \Psi}{\partial J_2} = 1, \quad \frac{\partial \Psi}{\partial J_3} + 2\frac{\partial \Psi}{\partial J_4} = 0.\tag{10}$$

Another constraint for the choice of the strain energy for residually stressed materials is that Ψ should have the same functional form for any configuration (as long as the deformation gradient $\mathbf{F}$ considered is elastic). This requirement results in a restriction called the *initial stress symmetry*, see Gower et al. (2015) for further details on this constitutive restriction.

In order to study the influence of residual stress on wave propagation, azimuthal shear, and torsion, Shams et al. (2011) and Merodio et al. (2013) proposed the following prototype constitutive equations:

$$\Psi = \tfrac{1}{2}\mu(I_1 - 3) + \tfrac{1}{2}(I_6 - I_{\tau 1}) + \tfrac{1}{2}\bar{\pi}(I_6 - I_{\tau 1})^2,$$
$$\Psi = \tfrac{1}{2}\mu(I_1 - 3) + \tfrac{1}{4}(I_5 - I_{\tau 1}),$$
$$\Psi = \tfrac{1}{2}\mu(I_1 - 3) + \tfrac{1}{2}(I_6 - I_{\tau 1}),\tag{11}$$

respectively, where $\mu, \bar{\pi}$ are material constants. Although they satisfy the conditions in Eq. (10), these candidates ignore the contribution of the invariants J_1, J_2, J_3, J_4, coupling the elastic deformation to the residual stresses, which is difficult to explain physically. Moreover, it turns out that they do not respect the initial stress symmetry (Gower et al., 2015).

An original approach is to take advantage of the existence of a virtual stress-free state, yet circumventing the need to actually define it from a kinematic viewpoint, as is done in Gower et al. (2015). There, the following strain energy density was found to satisfy both Eq. (10) and the initial stress symmetry:

$$\Psi = \Psi(I_1, J_1, I_{\tau 1}, I_{\tau 2}, I_{\tau 3}) = \tfrac{1}{2}\Big(J_1 + \tilde{p}I_1 - 3\mu\Big),\tag{12}$$

where $\mu > 0$ is a material parameter, and $\tilde{p} = \tilde{p}(I_{\tau 1}, I_{\tau 2}, I_{\tau 3})$ which we give an explicit representation for the plane stress case in the next section. It is worth noticing that in the absence of residual stress Ψ is the classical neo-Hookean strain energy function. Thus, Eq. (12) represents an extension of the neo-Hookean strain energy function for a residually stressed material, resulting in a function of only five of the nine independent invariants of $\mathbf{C}$ and τ. It is therefore expected that a functional dependence on the combined invariants J_2, J_3, J_4 would represent natural hyperelastic models of higher order.

3. Soft tubes under plane residual stresses: stability analysis

3.1. Plane residual stress

From now on we consider a soft hollow cylinder in the residually stressed reference configuration $\mathcal{B}_\tau$, indicating by R_i and R_o its inner and outer radii, respectively. Using a cylindrical coordinate system, the kinematics of the deformation can be defined by a mapping χ bringing the material point $\mathbf{X} = \mathbf{X}(R, \Theta, Z)$ to the spatial position $\mathbf{x} = \mathbf{x}(r, \theta, z) = \chi(\mathbf{X})$ in the deformed configuration, where (R, Θ, Z) and (r, θ, z) are the coordinates along the orthonormal vector bases $(\mathbf{E}_R, \mathbf{E}_\Theta, \mathbf{E}_Z)$ and

$(\mathbf{e}_r, \mathbf{e}_\theta, \mathbf{e}_z)$, respectively.

We consider that the cylinder behaves as a residually stressed neo-Hookean material described by Eq. (12), and assume a plane strain condition. This assumption simplifies the expression for $\tilde{p}$ greatly (Gower et al., 2015), as now it is given by the root of the quadratic

$$\tilde{p}^2 + \tilde{p}I_{\tau 1} + I_{\tau 3} - \mu^2 = 0. \tag{13}$$

Assuming also plane strain, the strain energy function of the pre-stressed body becomes

$$\Psi = \Psi(I_1, J_1, I_{\tau 1}, I_{\tau 3}) = \tfrac{1}{2}J_1 + \tfrac{1}{4}\left(\sqrt{I_{\tau 1}^2 + 4(\mu^2 - I_{\tau 3})} - I_{\tau 1}\right)I_1 - \mu, \tag{14}$$

where we have discarded the negative root of $\tilde{p}$ to ensure the positiveness of the strain energy function. From Eqs. (9) and (14), the Cauchy stress for the residually stressed tube reads

$$\tau = \tfrac{1}{2}\left(\sqrt{I_{\tau 1}^2 + 4(\mu^2 - I_{\tau 3})} - I_{\tau 1}\right)\mathbf{B} - \tilde{p}\mathbf{I} + \Sigma, \tag{15}$$

with $p_\tau = \tilde{p}(\mathbf{F} = \mathbf{I}) = \tfrac{1}{2}(\sqrt{I_{\tau 1}^2 + 4(\mu^2 - I_{\tau 3})} - I_{\tau 1})$ from Eq. (10)$_1$. Note that here and hereafter, tensors are two-dimensional, restricted to $\mathbf{E}_\alpha \otimes \mathbf{E}_\beta$ where $(\alpha, \beta) = (R, \Theta)$ in $\mathcal{B}_r$, and to $\mathbf{e}_i \otimes \mathbf{e}_j$ where $(i, j) = (r, \theta)$ in the current configuration $\mathcal{B}$.

3.2. Residual stress fields for the hollow cylinder

For the residually stressed hollow cylinder in its reference configuration $\mathcal{B}_r$, the equilibrium equations for the residual stress are

$$\left.\begin{aligned} \frac{\partial}{\partial R}\left(R^2\tau_{\Theta R}\right) + R\frac{\partial\tau_{\Theta\Theta}}{\partial\Theta} &= 0, \\ \frac{\partial}{\partial R}\left(R\tau_{RR}\right) + \frac{\partial\tau_{R\Theta}}{\partial\Theta} - \tau_{\Theta\Theta} &= 0, \end{aligned}\right\} \text{ for } R \in [R_i, R_o], \tag{16}$$

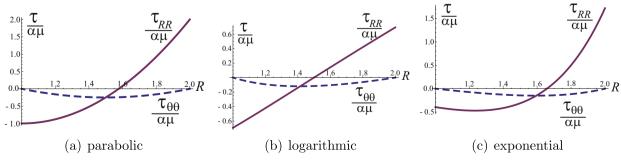complemented by the traction-free boundary conditions at the inner and outer radii,

$$\tau_{RR} = \tau_{R\Theta} = 0 \quad \text{for } R = R_i, \quad R = R_o, \tag{17}$$

We can write the general solution for Eq. (16) with the Airy stress function $\varphi = \varphi(R, \Theta)$, i.e. defining the residual stress components as

$$\tau_{RR} = \frac{1}{R}\varphi_{,R} + \frac{1}{R^2}\varphi_{,\Theta\Theta}, \quad \tau_{R\Theta} = \frac{1}{R^2}\varphi_{,\Theta} - \frac{1}{R}\varphi_{,\Theta R}, \quad \tau_{\Theta\Theta} = \varphi_{,RR}, \tag{18}$$

where the comma denotes partial differentiation. Eq. (18) allows an easy definition of different classes of self-equilibrated residual stresses for the tube, by simply imposing a functional dependence $\varphi(R, \Theta)$ respecting the boundary conditions in Eq. (17) and periodicity in Θ over 2π. This is a simpler approach than the one proposed by Rodriguez et al. (1994), which needed the a priori definition of the virtual stress-free state of the material to then define the mapping to the pre-stressed material configuration, followed by the a posteriori check if the resulting residual stress satisfies the equilibrium conditions.

When we take $\varphi = \varphi(R)$ only, we obtain a residual stress with diagonal terms only and the physical fields are axi-symmetric, which simplifies the analysis. Then

Fig. 1. Radial (solid purple lines) and hoop (dashed blue lines) residual stress components for a hollow cylinder with internal radius $R_i=1$ and external radius $R_o=2$. Here the stress potential is of parabolic (left), logarithmic (center), or exponential (right) form. (a) Parabolic. (b) Logarithmic. (c) Exponential. (For interpretation of the references to color in this figure caption, the reader is referred to the web version of this paper.)

$$\tau_{RR} = \frac{1}{R}f(R), \quad \tau_{\Theta\Theta} = f'(R), \quad \text{with } f(R_i) = f(R_o) = 0, \tag{19}$$

where $f(R) \equiv \varphi'(R)$ can be regarded as a *stress potential*.

In this paper we consider three representative residually stressed states in turn, as defined by the following variations for $f(R)$,

$$\begin{cases} (a) & f(R) = \alpha\mu R (R - R_i)(R - R_o)/R_i^2, \\ (b) & f(R) = \alpha\mu R \ln (R/R_i) \ln (R/R_o), \\ (c) & f(R) = \alpha\mu R \left(e^{R/R_i - 1} - 1 \right)\left(e^{R/R_o - 1} - 1 \right), \end{cases} \tag{20}$$

where α is a non-dimensional measure of the residual stress amplitude.

Fig. 1 depicts the corresponding radial and hoop residual stress variations through the thickness when $R_i = 1$, $R_o = 2$, normalized with respect to $\alpha\mu$. When $\alpha > 0$, the radial stress increases from the inner to the outer face, and it decreases when $\alpha < 0$. We call these situations *tensile* and *compressive residual stress*, respectively. As the magnitude $|\alpha|$ increases, the stress difference between the inner and the outer face can be so large as to de-stabilise the tube, as we see in the next section.

3.3. Incremental equations

We first investigate the stability of the residually stressed tube with the method of incremental deformations superposed on a finite field (Ogden, 1997), here a finite residual stress in contrast to other studies with a finite pre-strain. We perturb the residually stressed, axi-symmetric reference configuration by applying a two-dimensional incremental displacement vector **u**, expressed as

$$\mathbf{u} = u(R, \Theta)\mathbf{E}_R + v(R, \Theta)\mathbf{E}_\Theta, \tag{21}$$

where u, v are the incremental radial and hoop displacement fields, respectively. The spatial displacement gradient associated with the incremental deformation, $\mathbf{\Gamma} = \text{Grad}\,\mathbf{u}$, reads

$$\mathbf{\Gamma} = \begin{bmatrix} u_{,R} & (u_{,\Theta} - v)/R \\ v_{,R} & (v_{,\Theta} + u)/R \end{bmatrix}, \tag{22}$$

while the incremental constraint of incompressibility is

$$\text{tr }\mathbf{\Gamma} = 0. \tag{23}$$

The components of **s**, the linearised nominal stress on the reference configuration $\mathcal{B}_\tau$, are

$$s_{ij} = \mathcal{A}_{0ijkl}\Gamma_{lk} + p_\tau\Gamma_{ij} - q_\tau\delta_{ij}, \tag{24}$$

for $i, j = R, \Theta$, where q_τ is the increment of the Lagrange multiplier p_τ and $\mathcal{A}_0$ is the fourth-order tensor of instantaneous elastic moduli. Following Shams et al. (2011), we express its components for a residually stressed material as

$$\mathcal{A}_{0iklj} = \frac{\partial^2\Psi}{\partial F_{k\alpha}\partial F_{j\beta}} = 2\delta_{jk}\delta_{il}\Psi_1 + \delta_{jk}\tau_{il}, \tag{25}$$

where we take $\mathbf{F} = \mathbf{I}$ after differentiation, δ is the Kronecker delta and

$$\Psi_1 \equiv \frac{\partial\Psi}{\partial I_1} = \frac{1}{4}\sqrt{4\mu^2 + \left[\frac{1}{R}f(R) - f'(R) \right]^2} - \frac{1}{R}f(R) - f'(R). \tag{26}$$

The incremental equations of equilibrium are

$$\text{Div }\mathbf{s} = \mathbf{0}, \tag{27}$$

whilst the vanishing of the incremental traction at the free surface reads

$$\mathbf{s}^T\mathbf{E}_R = \mathbf{0} \quad \text{at } R = R_i, \ R_o. \tag{28}$$

3.4. Stroh formulation and surface impedance method

Assuming a cosine variation of u on the faces of the tube: $u(R, \Theta) = U(R) \cos (m\Theta)$, and then using Eqs. (24) and (22) we reach the following expressions for the incremental displacement and stress field,

$$[u(R, \Theta), s_{RR}(R, \Theta), q(R, \Theta)] = [U(R), S_{RR}(R), Q(R)] \cos{(m\Theta)},$$

$$[v(R, \Theta), s_{R\Theta}(R, \Theta)] = [V(R), S_{R\Theta}(R)] \sin{(m\Theta)}, \tag{29}$$

where the integer number m is the circumferential wavenumber, and the amplitudes U, V, S_{RR}, $S_{R\Theta}$, Q are scalar functions of R only. We now rewrite the governing equations in a Stroh (1962) formulation: a system with many favourable properties to solve boundary value problems. The first line of the Stroh form Eq. (30) below is just Eq. (23) reordered. The second line is a rewrite of Eq. (24) for the component $S_{R\Theta}$. Then we use the first two lines of Eq. (30) to substitute U' and V' in terms of U, V, S_{RR} and $S_{R\Theta}$ into Eq. (27), from which we get the third and fourth line of Eq. (30), resulting in

$$\frac{d}{dR}\begin{bmatrix} \mathbf{U} \\ R\mathbf{S} \end{bmatrix} = \frac{1}{R}\begin{bmatrix} \mathbf{G}_1 & \mathbf{G}_2 \\ \mathbf{G}_3 & -\mathbf{G}_1^T \end{bmatrix}\begin{bmatrix} \mathbf{U} \\ R\mathbf{S} \end{bmatrix} \quad \text{with} \quad \begin{cases} \mathbf{U}(R) = [U(R), V(R)]^T, \\ \mathbf{S}(R) = [S_{RR}(R), S_{R\Theta}(R)]^T, \end{cases} \tag{30}$$

where the sub-blocks of the Stroh matrix have the following components:

$$\mathbf{G}_1 = \begin{bmatrix} -1 & -m \\ \dfrac{2mR\Psi_1}{f + 2R\Psi_1} & \dfrac{2R\Psi_1}{f + 2R\Psi_1} \end{bmatrix}, \quad \mathbf{G}_2 = \begin{bmatrix} 0 & 0 \\ 0 & \dfrac{R}{f + 2R\Psi_1} \end{bmatrix},$$

$$\mathbf{G}_3 = \begin{bmatrix} 8\Psi_1 + (1 + m^2)f' + \dfrac{f[f + 2(1 + m^2)R\Psi_1]}{R(f + 2R\Psi_1)} & m\left[8\Psi_1 + 2f' + \dfrac{f(f + 4R\Psi_1)}{R(f + 2R\Psi_1)}\right] \\ m\left[8\Psi_1 + 2f' + \dfrac{f(f + 4R\Psi_1)}{R(f + 2R\Psi_1)}\right] & 8m^2\Psi_1 + (1 + m^2)\left(f' + \dfrac{f}{R}\right) - \dfrac{f^2}{R(f + 2R\Psi_1)} \end{bmatrix}, \tag{31}$$

which can be found be specialising the general expressions of Destrade et al. (2009, 2010) to the present context. Here we substituted $p_\tau = \mathcal{A}_{01212} - \tau_{RR}$ by using Eq. (10)$_1$ and Eq. (25), and substituted Q by using Eq. (24) with $i = j = R$.

We can solve numerically the boundary value problem formed by Eqs. (28) and (30) in a robust manner by adopting the *impedance matrix method*. Following Destrade et al. (2009) we introduce a functional relation between the incremental traction and the displacements vectors as

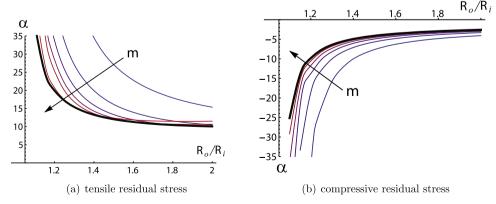$$R\,\mathbf{S}(R) = \mathbf{Z}(R)\,\mathbf{U}(R), \tag{32}$$

where $\mathbf{Z}$ is a *surface impedance matrix*. Substituting Eq. (32) into Eq. (30), we derive the following differential Riccati equation for $\mathbf{Z}$,

$$\frac{d}{dR}\mathbf{Z} = \frac{1}{R}(\mathbf{G}_3 - \mathbf{G}_1^T\mathbf{Z} - \mathbf{Z}\mathbf{G}_1 - \mathbf{Z}\mathbf{G}_2\mathbf{Z}), \tag{33}$$
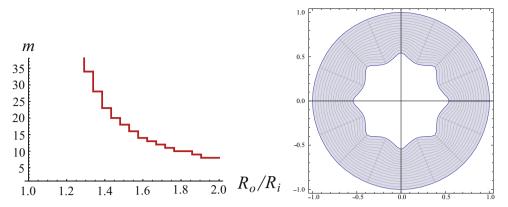
It must be integrated numerically from the initial condition $\mathbf{Z} = \mathbf{Z}(R_i) = \mathbf{0}$ (or, equivalently, $\mathbf{Z} = \mathbf{Z}(R_o) = \mathbf{0}$), to the target condition,

$$\det\mathbf{Z}(R_o) = \mathbf{0} \quad (\det\mathbf{Z}(R_i) = \mathbf{0}, \text{ respectively}). \tag{34}$$

Also in general $\mathbf{Z} = \mathbf{Z}^T$, see Shuvalov (2003).

Fig. 2. Instability curves for parabolic radial residual stress when $m = 2,5,8,11,14, 26$ (left) and when $m = 20, 30, \ldots, 70$ (right). In both cases m increases as the curves shade from blue to red. The thick black line represents the smallest value of $|\alpha|$ for instability to occur versus the aspect ratio R_o/R_i of the tube. (a) tensile residual stress. (b) Compressive residual stress. (For interpretation of the references to color in this figure caption, the reader is referred to the web version of this paper.)

Fig. 3. Critical circumferential wavenumber m for tensile parabolic residual stress versus the aspect ratio R_o/R_i of the tube (left). Solution of the incremental problem for the wrinkled tube (right) at $R_o = 1$, $R_i = 0.5$; resulting in the critical wavenumber is $m = 8$.

Once f, Ψ, R_o and R_i are prescribed for a given tube, we adjust the remaining parameter α, proportional to the amplitude of the residual stress, until we meet the target Eq. (34). Once α is determined, we can integrate the first line of Eq. (30), i.e.

$$\frac{d\mathbf{U}}{dR} = \frac{1}{R}\mathbf{G_1}\mathbf{U} + \frac{1}{R}\mathbf{G_2}\mathbf{Z}\mathbf{U}, \tag{35}$$

simultaneously with Eq. (33) to compute the incremental displacement field throughout the thickness of the tube wall.

The numerical method for solving the initial value problem given by Eqs. (33) and (34) for the three potential stress functions in Eq. (20) is presented in the next section.
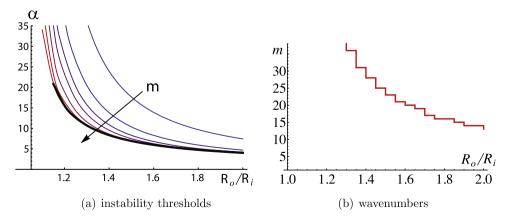
3.5. Numerical results on wrinkling

The Hamiltonian structure and algebraic properties of the Stroh matrix yield a robust numerical procedure to determine when wrinkles appear on either of the faces of the residually stressed tube (Fu, 2007; Shuvalov, 2003). Here we find the unique, symmetric, semi-definite solution of the differential Riccati equation for $\mathbf{Z}$ in Eq. (33) by numerical integration using the software *Mathematica* (Wolfram Inc., version 10.1, Champaign, IL) from the initial zero value to a target condition given by the boundary condition in Eq. (34).
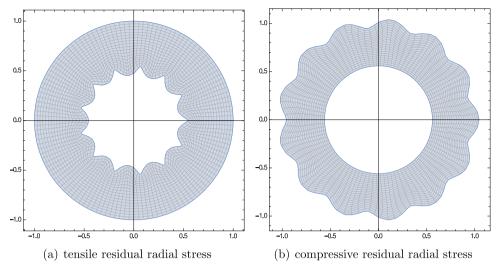
We consider in turn the three expressions for $f(R)$ in Eq. (20). In each case we consider μ to be constant and find the critical value $\alpha > 0$ ($\alpha < 0$) for wrinkles to appear on the inner face (outer face), under tensile (compressive) residual stress.

For the parabolic stress potential $f(R) = \alpha\mu R(R - R_i)(R - R_o)/R_i^2$, the instability curves are depicted for various wavenumbers in Fig. 2. In particular, we find that for both positive and negative values of α, the instability curves depend strongly on the aspect ratio of the tube (see Fig. 2). The critical wavenumbers for positive α (tensile residual stress) are shown in Fig. 3(a), with the corresponding in-plane wrinkles on the inner face when $R_o/R_i = 2$ shown in Fig. 3(b).

For the logarithmic stress potential $f(R) = \alpha\mu R \ln(R/R_i)\ln(R/R_o)$, the instability curves occur at the same absolute value of α, so that a single figure is required to display the results for both tensile and compressive residual stresses, see Fig. 4(a).

(a) instability thresholds   (b) wavenumbers

Fig. 4. Instability curves (solid lines) for logarithmic residual stress potential shown at $m = 2, 5, 8, 11, 17, 26, 38$, where the curves shade from blue to red as m increases. The thick black line represents the critical values of the residual stress amplitude α versus the aspect ratio R_o/R_i of the tube (left). Critical circumferential wavenumber m versus the aspect ratio R_o/R_i of the tube (right). (a) Instability thresholds. (b) Wavenumbers. (For interpretation of the references to color in this figure caption, the reader is referred to the web version of this paper.)
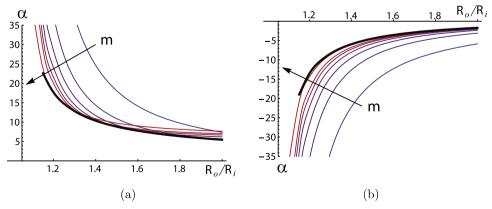
Fig. 5. Solution of the incremental problem for the tube with logarithmic residual stress potential when $R_o=1$, $R_i=0.5$, shown for tensile (left) and compressive (right) residual stresses. Here the critical circumferential wavenumber is $m=13$. (a) Tensile residual radial stress. (b) Compressive residual radial stress. (For interpretation of the references to color in this figure caption, the reader is referred to the web version of this paper.)

We note that the solution in the compressive case $\alpha < 0$, with its wrinkles on the outer face, is reminiscent of the one proposed by Dervaux and Ben Amar (2011) for the edge buckling of a growing thin ring of gel enclosing a hard disc. See Fig. 5 for an example of two wrinkled configurations. Finally, the results for the exponential stress potential $f(R) = \alpha\mu R(e^{R/R_i-1} - 1((e^{R/R_o-1} - 1)$, are qualitatively similar to those of the parabolic case, with instability curves depicted in Fig. 6.

In particular, the critical circumferential wavenumber m of the instability for the positive values of α is depicted in Fig. 7 (left), whilst its incremental solution for the wrinkled tube is shown in Fig. 7(right).
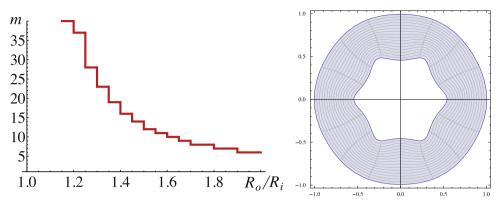
In the next section, we use the critical thresholds calculated by solving the incremental elastic problem as the basis from which to perform a numerical post-buckling investigation of the fully nonlinear morphology of the residually stressed tube.

4. Numerical post-buckling simulations

In this Section, we investigate numerically the morphology of the residually stressed tube when the parameter α, governing the intensity of the residual stress distribution, goes beyond the linear stability threshold of wrinkling. First, we describe the implementation of a numerical finite element method, validating the simulation results with the theoretical predictions for the linear stability thresholds. Second, we investigate the morphology of the residually stressed tubes in the post-buckling regime for the three cases of stress potential (parabolic, logarithmic, exponential).

Fig. 6. Instability curves (solid lines) for exponential residual stress potential shown at $m = 2, 5, 8, 11, 14, 17, 29$ for the positive (left) and negative (right) values of the residual stress amplitude α. The thick black line represents the lowest critical values of $|\alpha|$ for the onset of wrinkles versus the aspect ratio R_o/R_i of the tube.

Fig. 7. Critical circumferential wavenumber m for positive values of the critical amplitude α, using an exponential stress potential versus the aspect ratio R_o/R_i of the tube (left). Solution of the incremental problem for a tube with $R_o = 1$, $R_i = 0.5$, and the critical wavenumber is $m = 6$.

4.1. Description of the numerical model

We implement the mixed variational formulation of the neo-Hookean model with residual stress (Eq. (12)) into the open source code FEniCS (Logg et al., 2012). We consider a hollow cylinder with $R_o = 1.0$ and $R_i = 0.5$ as the initial 2D geometry. We perform quasi-static simulations using triangular *Mini* elements, where the displacements are discretized with piecewise linear functions enriched by cubic bubble functions, whereas the pressure is discretized by continuous piecewise linear functions.
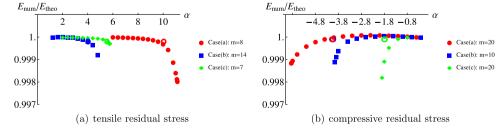
To avoid rigid motions, we impose null displacements for all the points of the external (internal) boundary in the case of positive (negative) values of α. We check *a posteriori* the effect of this kinematic constraint compared with the stress-free condition considered theoretically. In all numerical simulations we find indeed that the radial stress is zero at the fixed boundary, even in the post-buckling regime.

For the onset of localized instabilities, we follow Ciarletta et al. (2014) and impose an initial sinusoidal imperfection with a prescribed mode m and amplitude 0.0025 on the inner (outer) face nodes for α positive (negative), corresponding to the incremental wrinkles of Section 3. The finite element model is then solved using a incremental iterative Newton–Raphson method over the control parameter α, with an automatic adaptation of the step size.
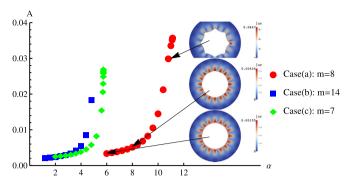
4.2. Validation versus the theoretical predictions

We validate the numerical model by comparing it against the stability curves from the theoretical analysis of Section 3. For this purpose, the numerical thresholds α_{sim}^{th} is computed as the values of α such that the ratio between the total energy of the system computed numerically, E_{num}, and theoretically, E_{theo}, (i.e. for the axi-symmetric solution) is $E_{num}/E_{theo} = 0.9999$.

Fig. 8(a) depicts the ratio E_{num}/E_{theo} versus $\alpha > 0$ for the three cases of residual stress Eq. (12). The mode m of the initial imperfection in each simulation has been chosen as the most critical condition predicted theoretically. Fig. 8(b) shows the energy ratio in function of negative values of α. Then, the mode m of the initial imperfection has been chosen arbitrarily for the sake of graphical clarity, since the unstable wavelength is very short. The theoretical values (indicated by circles in Fig. 8) are also reported, highlighting the good agreement of the numerical results with the theoretical predictions. We notice that a certain discrepancy arises when considering the negative critical values, although the theoretical predictions are well within the ratio $E_{num}/E_{theo} = 0.999$. This difference may indicate that the corresponding bifurcations are more sensitive to the initial imperfections, especially since we do not implement any damping methods for stabilizing the post-buckling solution, in order to avoid artificial behaviors.

Fig. 8. Energy ratio E_{num}/E_{theo} versus α for the three choices of residual stress fields in Eq. (20), when $R_o/R_i = 2.0$ and α is either positive (a) or negative (b). The hollow circles indicate the theoretical predictions for the stability boundary thresholds. The theoretical and simulated linear stability thresholds are, in (a): $\alpha_{theo}^{th} = 10.05$; $\alpha_{sim}^{th} = 9.62$ (blue discs); $\alpha_{theo}^{th} = 4.02$; $\alpha_{sim}^{th} = 4.00$ (red squares); $\alpha_{theo}^{th} = 5.53$; $\alpha_{sim}^{th} = 5.55$ (black diamonds); in (b): $\alpha_{theo}^{th} = -4.07$; $\alpha_{sim}^{th} = -4.2$ (blue discs); $\alpha_{theo}^{th} = -4.05$; $\alpha_{sim}^{th} = -3.3$ (red squares); $\alpha_{theo}^{th} = -1.79$; $\alpha_{sim}^{th} = -1.3$ (black diamonds). (a) Tensile residual stress. (b) Compressive residual stress. (For interpretation of the references to color in this figure caption, the reader is referred to the web version of this paper.)

Fig. 9. Amplitude evolution of the initial perturbation for the three cases investigated when the control parameter α is positive (tensile residual stress). The deformed morphology is also presented for three indicative values of α in the case of residual stress of parabolic type.

4.3. Residually stressed morphology in the post-buckling regime

Once it has been validated, we use the proposed numerical method to investigate the morphology of the residually stressed configuration when the order parameter α is far beyond the linear stability threshold.

Fig. 9 depicts the amplitude A of the post-buckling patterns emerging in the numerical simulations for positive values of α in the three cases of residual stress given by Eq. (20). We remark that there is a continuous transition from a wrinkled to a folded pattern, which is indicative of a subcritical bifurcation. In Table 1 we display the morphological phase diagram for the tube in either positive and negative values of α.

Finally, we remark that the incompressibility constraint for the implemented elements is imposed in a weak sense. As a consequence, the morphological transition in the tube can induce a slight shrinkage or enlargement of the boundary elements, eventually creating an excessive distortion and blocking the simulations. Thus, future numerical improvements can be concerned with the implementation of an element-wise formulation of the incompressibility constraint.

5. Discussion and concluding remarks

We used a recently proposed constitutive model to examine first the equilibrium and next the destabilization of soft tubular materials with increasing levels of residual stresses.
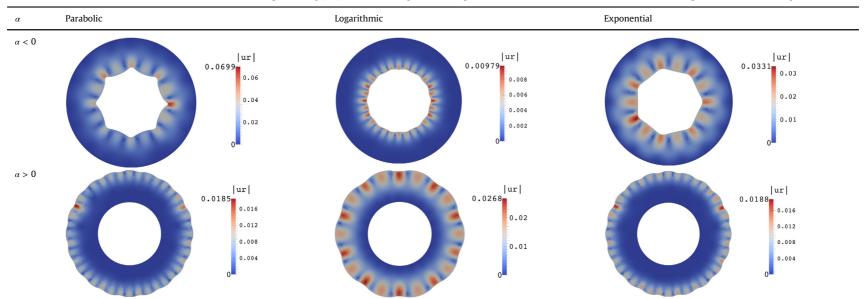
We saw that under plane residual stress, the components of the elastic Cauchy stress tensor can be expressed as a function of a stress potential, which allows a straightforward simplification of the problem in the axi-symmetric case. In particular, we focused on three different residual stress distributions (parabolic, logarithmic, an exponential), and investigated the stability of the resulting pre-stressed configurations using a mix of analytical and numerical techniques.

First, we employed the theory of incremental deformations to study the onset of an elastic bifurcation. Using the Stroh formulation and the surface impedance method, the incremental boundary value problem was transformed into the differential Riccati equation (33) with initial conditions (34), which can be solved by implementing a robust numerical procedure. The resulting marginal stability curves for the three cases are shown in Figs. 2–7, together with the bifurcated morphologies. In particular, we demonstrated that the emerging patterns are localised at the free surface having a threshold compressive value of the hoop residual stress, strongly depending on the ratio between the outer and inner radii. These patterns can arise on the inner (in the case of a tensile residual stress) as well as on the outer (in the case of a compressive residual stress) faces of the tube.

Second, we implemented a novel finite element code of the proposed model in order to study the post-buckling evolution of the emerging morphology. We validated the numerical code by checking the linear stability thresholds for the onset of buckling, and we derived the post-buckling morphologies in the three cases of residual stress under consideration. In particular, we have shown that the accumulation of a compressive hoop residual stress in the fully nonlinear regime drives the transition from a wrinkled to a creased state, which is typically observed in several tubular organs (Ciarletta et al., 2014).

The results of this study may have important applications for the non-destructive determination of the residual stress distribution in soft tubular tissues. Existing approaches aim at deriving the virtual stress-free state by performing multiple cuttings, possibly an infinity of them (e.g. Lu et al., 2003; Dou et al., 2006). By contrast, our method and results allow to correlate directly the geometrical parameters of the wrinkled or creased morphology with the spatial distribution of the underlying residual stress components. Thus, we open a novel perspective for guiding the use of non-invasive techniques for measuring the residual stresses within living matter. It can be connected to the non-destructive evaluation of a residual stress distribution by means of elastic waves (Man and Lu, 1987; Shams et al., 2011). Future works can be devoted to improve the constitutive model in order to take into account more complex material behaviors, e.g. describing the elasticity of real

Table 1
The result of finite element simulations for the residual stresses given in Eq. (20) with either the positive or negative critical value for α. The scalebars indicate the magnitude of the radial displacement.

α	Parabolic	Logarithmic	Exponential
$\alpha < 0$			
$\alpha > 0$			

biological networks (Storm et al., 2005), and incorporating slight compressibility (Gower et al., 2015), heterogeneity (Ciarletta et al., 2014) and structural anisotropy, which is almost ubiquitous in tubular organs (Gasser et al., 2006).

Acknowledgments

References

Bao, G., Suresh, S., 2003. Cell and molecular mechanics of biological materials. Nat. Mater. 2 (11), 715–725.
Chuong, C., Fung, Y., 1986. Residual stress in arteries. In: Frontiers in Biomechanics. Springer, New York, pp. 117–129.
Ciarletta, P., Balbi, V., Kuhl, E., 2014. Pattern selection in growing tubular tissues. Phys. Rev. Lett. 113 (24), 248101.
Dervaux, J., Ben Amar, M., 2011. Buckling condensation in constrained growth. J. Mech. Phys. Solids 59 (3), 538–560.
Destrade, M., Murphy, J.G., Ogden, R.W., 2010. On deforming a sector of a circular cylindrical tube into an intact tube: existence, uniqueness, and stability. Int. J. Eng. Sci. 48, 1212–1224.
Destrade, M., Nì Annaidh, A., Ciprian, C.D., 2009. Bending instabilities of soft biological tissues. Int. J. Solids Struct. 46, 4322–4330.
Dou, Y., Fan, Y., Zhao, J., Gregersen, H., 2006. Longitudinal residual strain and stress–strain relationship in rat small intestine. Biomed. Eng. Online 5, 37.
Fu, Y., 2007. Hamiltonian interpretation of the Stroh formalism in anisotropic elasticity. Proc. R. Soc. Ser. A 463 (2088), 3073–3087.
Gasser, T.C., Ogden, R.W., Holzapfel, G.A., 2006. Hyperelastic modelling of arterial layers with distributed collagen fibre orientations. J. R. Soc. Interface 3 (6), 15–35.
Gower, A.L., Ciarletta, P., Destrade, M., 2015. Initial stress symmetry and its applications in elasticity. Proc. R. Soc. Ser. A 471, 20150448.
Hoger, A., 1985. On the residual stress possible in an elastic body with material symmetry. Arch. Rational Mech. Anal. 88 (3), 271–289.
Hoger, A., 1986. On the determination of residual stress in an elastic body. J. Elast. 16 (3), 303–324.
Hoger, A., 1993. Residual stress in an elastic body: a theory for small strains and arbitrary rotations. J. Elast. 31 (1), 1–24.
Hoger, A., 1996. The elasticity tensor of a transversely isotropic hyperelastic material with residual stress. J. Elast. 42 (2), 115–132.
Johnson, B.E., Hoger, A., 1993. The dependence of the elasticity tensor on residual stress. J. Elast. 33 (2), 145–165.
Logg, A., Mardal, K.-A., Wells, G., 2012. Automated Solution of Differential Equations by the Finite Element Method: The FEniCS Book, vol. 84. Springer Science & Business Media, Berlin, Heidelberg.
Lu, X., Yang, J., Zhao, J., Gregersen, H., Kassab, G., 2003. Shear modulus of porcine coronary artery: contributions of media and adventitia. AJP Heart Circul. Physiol. 285 (5), H1966–H1975.
Man, C.-S., Lu, W., 1987. Towards an acoustoelastic theory for measurement of residual stress. J. Elast. 17, 159–182.
Merodio, J., Ogden, R.W., Rodríguez, J., 2013. The influence of residual stress on finite deformation elastic response. Int. J. Non-Linear Mech. 56, 43–49.
Ogden, R.W., 1997. Non-linear Elastic Deformations. Dover Publications, New York.
Rodriguez, E.K., Hoger, A., McCulloch, A.D., 1994. Stress-dependent finite growth in soft elastic tissues. J. Biomech. 27 (4), 455–467.
Shams, M., Destrade, M., Ogden, R.W., 2011. Initial stresses in elastic solids: constitutive laws and acoustoelasticity. Wave Motion 48 (7), 552–567.
Shuvalov, A., 2003. A sextic formalism for three-dimensional elastodynamics of cylindrically anisotropic radially inhomogeneous materials. Proc. R. Soc. Ser. A 459 (2035), 1611–1639.
Skalak, R., Zargaryan, S., Jain, R.K., Netti, P.A., Hoger, A., 1996. Compatibility and the genesis of residual stress by volumetric growth. J. Math. Biol. 34 (8), 889–914.
Storm, C., Pastore, J.J., MacKintosh, F.C., Lubensky, T.C., Janmey, P.A., 2005. Nonlinear elasticity in biological gels. Nature 435 (7039), 191–194.
Stroh, A.N., 1962. Steady state problems in anisotropic elasticity. J. Math. Phys. 41 (2), 77–103.